Theor Chem Acc (2012) 131:1123
DOI 10.1007/s00214-012-1123-0

REGULAR ARTICLE

$O + C_2H_4$ potential energy surface: excited states and biradicals at the multireference level

Aaron C. West · Joseph D. Lynch · Bernhard Sellner · Hans Lischka · William L. Hase · Theresa L. Windus

Received: 4 September 2011 / Accepted: 26 October 2011 / Published online: 15 February 2012

Abstract The focus of this study is to understand the multiconfigurational nature of the biradical species involved in the early reaction paths of the oxygen plus ethylene PES. In previous work (J Phys Chem A 113, 12663, 2009), the lowest-lying $O(^3P) + C_2H_4$ PES was extensively explored at the MCSCF, MRMP2, and MR-AQCC levels of theory. In the current work, ground and excited, triplet- and singlet-state reaction paths for the initial addition of oxygen to ethylene were found at the MCSCF and MRMP2 levels along with five singlet pathways near the $^{\cdot}CH_2CH_2O^{\cdot}$ biradical at the MCSCF, MRMP2, and CR-CC(2,3) levels. One of these five paths can lead to the $CH_2CO + H_2$ products from CH_3CHO rather than from the $^{\cdot}CH_2CH_2O^{\cdot}$ biradical, and this pathway was investigated with a variety of CAS sizes. To provide further comparison between the MRMP2 and CR-CC(2,3) levels, MR-AQCC single-point energies and optimizations were performed for select geometries. After the initial exploration of this region of the surface, the lowest singlet–triplet surface crossings were explicitly determined at the MCSCF level. Additional MRMP2 calculations were performed to demonstrate the limitations of single-state perturbation theory in this biradical region of the PES, and SO-MCQDPT2 single-point energies using SA MCSCF were calculated on a grid of geometries around the primary surface crossing. In particular, these calculations were examined to determine a proper active space and a physically reasonable number of electronic states. The results of this examination show that at least four states must be considered to represent this very complex region of the PES.

Keywords Multireference · Spin–orbit coupling · Potential energy surface · Biradical · Combustion

Electronic supplementary material The online version of this article (doi:10.1007/s00214-012-1123-0) contains supplementary material, which is available to authorized users.

A. C. West · T. L. Windus (✉)
Department of Chemistry, Iowa State University, Ames, IA 50011, USA
e-mail: twindus@iastate.edu

J. D. Lynch
School of Medicine, Robert C. Byrd Health Sciences Center, P.O. Box 9100, Morgantown, WV 26506-9600, USA

B. Sellner · H. Lischka
Institute for Theoretical Chemistry, University of Vienna, Waehringerstrasse 17, 1090 Vienna, Austria

H. Lischka · W. L. Hase
Department of Chemistry and Biochemistry, Texas Tech University, Memorial Circle and Boston, Lubbock, TX 79409-1061, USA

1 Introduction

Understanding the kinetics and dynamics of the O + ethylene reaction is important for both hydrocarbon combustion studies [2] and development of materials that resist surface erosion for space vehicles in low-Earth orbit. Several low-pressure crossed molecular beam experiments [3–5] were performed for this reaction. On the lowest-lying triplet potential energy surface (PES), $O(^3P)$ addition to ethylene first forms a ketocarbene that connects to reaction pathways leading to the three most dominant set of products $CH_2CHO + H$, $CH_3 + CHO$, and $CH_2 + H_2CO$ [6]. The pathways to the CH_2CHO and H_2CO products are low barrier, single-step decompositions, and these reactions occur under thermal conditions. In contrast, the CHO

reaction channel has a large rearrangement barrier prior to decomposition and is only observed for hyperthermal reactant conditions. In the vicinity of the triplet ketocarbene, triplet–singlet non-adiabatic electronic transitions are possible to the singlet PES. If this electronic transition occurs, a hydrogen shift leads to the $CH_3 + HCO$ products.

The overall product distributions are nearly pressure independent over a temperature range of 287–2,000 K and a pressure range of 0.007–1 atm [6]. Nguyen et al. [6] have shown that collisional stabilization of the ketocarbene adduct remains negligible (<10%) even at 100 atm and ~1,500 K. Thus, the product distributions are primarily controlled by the temperature. As found from both theoretical calculations [6] and experiment [3], at 298 K the percentage yields for the three dominant channels (i.e., $CH_2CHO + H$, $CH_3 + CHO$, and $CH_2 + H_2CO$) are 40 ± 10, 50 ± 10, and 10 ± 5, respectively. For the much higher temperature of 2,000 K, theoretical calculations give percentages of 18.5, 36.9, and 29.1 for the respective yields of these three products [6]. As the temperature is varied, both the product yields and distributions change.

Several initial theoretical studies of this reaction are present in the literature [7–11]. This work was followed by the calculations of Nguyen et al. [6] considered above and those of Hu et al. [12], who studied the reaction in substantial detail at different levels of theory on both the triplet and singlet PESs. In addition, Joshi et al. [13] studied oxirane decomposition with B3LYP/6-311++G(d, p) optimized geometries and G3B3/6-311++G(d, p) single-point energies and investigated the biradical region of the singlet PES with an unrestricted singlet wavefunction and spin projection. Yang et al. [14] located ~100 stationary points involved in reactions that emanate from the acetaldehyde potential energy minimum. They used B3LYP/6-311++G(d, p) geometries and CCSD(T)/cc-pVTZ single-point energies with basis set superposition error corrections for weakly bound complexes. Recent studies at the CCSD(T)/aug-cc-pVTZ level of theory by Bowman investigated how pathways important to the $CH_4 + CO$ product channel bypass the minimum energy path (MEP) and hence the traditional transition state (TS) [15–17]. Combining both experimental and theoretical results, another recent study [18] proposed a novel pathway (i.e., $^{\cdot}CH_2CH_2O^{\cdot} \rightarrow CH_2CO + H_2$). However, the theoretical component is somewhat uncertain since it consisted of G3(MP2) single-state, single-reference results with large spin contamination. To date, most theoretical studies on this system rely on single determinant methods since understanding even the most important reactions for this system proves to be a challenge for multireference electronic structure theory methods. The calculations presented here examine the multireference nature of the $O + C_2H_4$ reactions, which show several important non-adiabatic transitions in the biradical region.

For the O + ethylene reaction, both the two lowest-lying triplets and two lowest-lying singlets play important roles in the reactions of the initially formed biradicals and the ensuing dynamics. Our initial study [1] of the lowest-lying triplet PES examined pathways 1–9 from the Nguyen et al. [6] work as well as an additional path 10. The current study expands this earlier work [1] by examining multireference barriers for the lowest-lying singlet paths 10–13, 20 as labeled in Nguyen et al. [6], excited states for path 1, the Miyoshi path (M), and important surface crossings. In particular, this study examines the following reactions:

Triplet A′ 1) $^{\cdot\cdot}O(^3P) + C_2H_4 \rightarrow {}^{\cdot}CH_2CH_2O^{\cdot}$
Singlet A_1 1) $^{\cdot\cdot}O(^1D) + C_2H_4 \rightarrow$ oxirane
Singlet A″ 1) $^{\cdot\cdot}O(^1D) + C_2H_4 \rightarrow {}^{\cdot}CH_2CH_2O^{\cdot}$
10) $^{\cdot}CH_2CH_2O^{\cdot} \rightarrow CH_3CHO$
11) $^{\cdot}CH_2CH_2O^{\cdot} \rightarrow$ oxirane
12) $^{\cdot}CH_2CH_2O^{\cdot} \rightarrow CH_2CHOH$
13) $CH_3CHO \rightarrow$ oxirane
M) $^{\cdot}CH_2CH_2O^{\cdot} \rightarrow CH_2CO + H_2$
20) $CH_3CHO \rightarrow CH_2CO + H_2$.

.

2 Methods

Results from calculations at the multiconfigurational self-consistent field (MCSCF) level in combination with several dynamical correlation methods were obtained with the GAMESS software [19]. Since the multireference approach for these calculations has already been explained for the triplet surface [1], only a summary of that procedure is given here. To recover the majority of the quasi-degenerate correlation, all calculations were carried out at the full optimized reaction space (FORS) [20–22], or complete active space self-consistent field (CASSCF), level of theory using the aug-cc-pVTZ [23] basis set. The previous paper [1] compared calculations between aug-cc-pVTZ and aug-cc-pVDZ [23] and showed the double zeta basis set to be sufficient for this system. The determinant-based method [24] and the full Newton–Raphson converger with the augmented Hessian technique [25–27] were used because of the large complete active space (CAS) sizes and the biradical species. Restricted Hartree–Fock (RHF) or restricted open shell Hartree–Fock (ROHF) calculations with modified valence orbitals [28] and Boys localization [29] provided good starting orbitals in most situations. CASSCF stationary point searches for species in the reactions described above employed analytic gradients and central differenced, numerical Hessians. As in the first paper [1], second-order, Gonzalez–Schlegel (GS2) [30],

intrinsic reaction coordinate (IRC) calculations identified minima associated with each TS.

Once a reaction path was located, single-state multireference Møller–Plesset second-order perturbation theory (MRMP2) [31] as well as completely renormalized coupled-cluster singles, doubles, and non-iterative triples (CR-CC(2,3)) [32, 33] single-point energies using the aug-cc-pVTZ basis set were performed along the IRC to recover the majority of the dynamic correlation. In the previous work on the triplet surface, MRMP2 results quantitatively agreed with multireference average quadratic coupled-cluster (MR-AQCC) [34] results obtained using COLUMBUS [35–37]. Since both analytic gradients and Hessians at the MRMP2 level are unavailable in GAMESS, numerical derivatives are required. Unfortunately, numerical derivatives involve computation at asymmetric geometries where the multireference wavefunction might converge to any close-lying states by orbital root flipping (ORF) to a different active space. Thus, given that the MRMP2 results depend on the active space, geometry optimizations, IRCs, and Hessians at this level are numerically prohibitive and sometimes unfeasible.

To further validate the results, the COLUMBUS program [35–37] was used for GVB-PP and MR-AQCC single-point energy and geometry optimization calculations at select geometries with the cc-pVDZ [23] basis. The GVB-PP(9) approach utilizes the generalized valence bond-perfect pairing (GVB-PP) method with 9 electron pairs [38–40]. Besides the chemical core O1 s and C1 s orbitals, which are doubly occupied, all other orbitals are treated on an equal footing, allowing for the correct dissociation of individual electron pairs. The total electronic wave function consists of an antisymmetrized product of the nine perfect pairs (PPs), yielding a space of 2^9 (512) configurations. For the MR-AQCC calculations, a PP(5) reference space was chosen for path 12 and a PP(4) reference space for path 13. The choice of pairs was guided by considerations of the necessary orbitals for the reaction, balanced treatment of bonds, and computational cost. The bonding orbitals of the remaining pairs are doubly occupied in the reference space. For path 12, these doubly occupied orbitals represent two CH, the CC, and the CO bond, while in path 13 the four CH and the CC bonds are used. Based on these reference spaces, single and double excitations are allowed by imposing generalized interacting space restrictions [41]. With 32 (16) reference configuration state functions for PP(5) (PP(4)), the total MR-AQCC expansion space consists of 3,088,992 (1,561,728) configurations.

Even though most of the lowest-lying singlet PES lies far below the lowest-lying triplet surface, the $^{\cdot}CH_2CH_2O^{\cdot}$ biradical has several degenerate electronic states that can lead to non-radiative transitions and to several major singlet minima. To understand these electronic states, two minimum energy crossing (MEX) regions were located at the CASSCF level with GAMESS: one near the $^{\cdot}CH_2CH_2O^{\cdot}$ triplet minimum and one near the $^{\cdot}CH_2CHOH$ triplet biradical. Because calculations based on a single-state (8,7) CAS resulted in ORF, the crossing seam near $^{\cdot}CH_2CH_2O^{\cdot}$ was located with a (6,6) CAS, which yielded equal energy gaps at the CASSCF and MRMP2 levels between the lowest-lying triplet and lowest-lying singlet states at the triplet $^{\cdot}CH_2CH_2O^{\cdot}$ minimum; this specification ensures that both surfaces receive similar amounts of correlation at these levels of theory.

Investigating these PES regions requires both location of the crossing seams [42–44] and a multiple-state perturbation approach [45–48] with spin–orbit coupling (SOC) [49, 50]. Toward this end, second-order, spin–orbit multiconfigurational quasi-degenerate perturbation theory (SO-MCQDPT2) [50, 51] single-point energies were calculated with GAMESS at the CASSCF MEX geometries. The SO-MCQDPT2 level of theory combines spin–orbit effects of the partial or full Breit–Pauli operator [51–54] with MCQDPT2 [48]. The SO calculations included full 1-electron and partial 2-electron integrals, which result in a mean field adjustment to the 1-electron integrals. SO-CAS configuration interaction (SO-CASCI) energies are also reported since they are included in the SO-MCQDPT2 energy evaluation. The second-order, perturbative calculations included all excitations from the reference into the virtual space from all but the chemical core orbitals (O1 s, C1 s). Unlike the calculations with pure (i.e., single) state solutions, state averaged (SA) MCSCF can lead to appropriate active spaces that include the lone O2p without in–out correlation (IOC). So, with the proper electronic states, the SO-MCQDPT2 approach can lead to physically meaningful results.

To further investigate the multi-state nature of the $^{\cdot}CH_2CH_2O^{\cdot}$ biradical region, (8,7) SA CASSCF and SO-MCQDPT2, single-point energies were computed for the geometries previously obtained in the CASSCF IRCs near the biradical region. The number of electronic states included was primarily determined by examination of the energy gaps between the states for both pure and SA wavefunctions. In addition, around the $^{\cdot}CH_2CH_2O^{\cdot}$ MEX geometry, a series of (8,7) SA CASSCF and corresponding SO-MCQDPT2, single-point energies using geometries obtained from (6,6) CAS, triplet constrained optimizations were performed to further describe this very flat, 14-dimensional intersection seam.

3 Results and discussion

Table 1 displays the active space for each reaction where the label "far" refers to the carbon farthest from oxygen.

Table 1 Description of the main CAS sizes used for each reaction pathway

Reaction pathway	Active space	In–out correlation	Description
1 $^3A''$	(6,6)	N	CCσ, CCπ, biradical(2O2p)
1 $^3A'$			→ CCσ, COσ, biradical(farC2p, O2p)
1 $^1A''$			
1 $^1A_1$	(6,6)	N	CCσ, CCπ, biradical(2O2p)
			→ CCσ, 2COσ
10	(14,14)	N	4 CHσ, CCσ, COσ, biradical(farC2p, O2p)
			→ 4 CHσ, CCσ, COσ, COπ
11	(6,6)	N	COσ, CCσ, biradical(farC2p, O2p)
			→ 2 COσ, CCσ
12	(10,10)	N	COσ, CCσ, 2 CHσ, biradical(farC2p, O2p)
			→ COσ, CCσ, CHσ, OHσ, CCπ
13	(10,10)	Y	CHσ, COσ, COπ, CCσ, lone O2p
			→ CHσ, 2 COσ, CCσ, lone O2p
M	(10,10)	N/A	2 CHσ, COσ, CCσ, biradical(farC2p, O2p)
			→ ORF for the O2p
20	(12,12)	Y	2 CHσ, COπ, lone O2p, COσ, CCσ
			→ HHσ, 2 COπ, CCπ, COσ, CCσ,

Only the lone pairs and bonding orbitals are shown; the antibonding orbitals can be inferred from bonding orbitals and the indication of in–out correlation. The O2 s is always in the core

Examination of bond length changes, natural orbital occupation numbers, and localized molecular orbital coefficients in different CAS sizes over the course of each reaction ultimately decide the choice of the final active space. Tables 2 and 3 give the overall barrier information for all elementary reactions listed in the Introduction where each TS divides each pathway into a forward barrier (reactant to TS) and a reverse barrier (product to TS). Table 2 shows the CAS barriers with and without zero-point energies (ZPE). Table 3 contains energetics at several levels of theory: (1) the barriers from single-point MRMP2 energies along the CASSCF IRCs; (2) optimized MR-AQCC barriers for paths 12 and 13; (3) Nugyen et al. [6] and Yang et al. [14] barriers; (4) single-point MR-AQCC barriers along the CASSCF IRC for paths 12 and 13; and (5) the barriers from single-point CR-CC(2,3) energies along the CASSCF IRCs. While the single-point energies along the CASSCF IRC geometries are not strictly barriers, they should approximate the barriers [1]. Differences between single-point MRMP2 data at the MCSCF minima and maxima are labeled stationary point MRMP2 (SPMRMP2) energy barriers and always include ZPE (except for species with ORF issues in numerical Hessians as discussed below). However, as shown below, single-point MRMP2 energies along the IRC can result in shifted barriers because of shifts in the TS and/or the minimum(a) (i.e., reaction coordinate/horizontal shifts and energetic/vertical shifts).

As in our first paper [1], results with IOC tend to incorporate more dynamic correlation into the reference wavefunction. However, if a weakly occupied IOC orbital undergoes ORF with a virtual orbital and if dynamic correlation has a large contribution to the total correlation, then barriers with different IOC orbitals do not necessarily lead to accurate energetics. Therefore, IOC orbitals in the active space might result in configurations that lead to unphysical barriers. As a result, unless either the IOC constitutes proper radial correlation at some geometry in the pathway or ORF prevents placing the lone O2p in the MCSCF core, CASSCF active spaces do not contain IOC orbitals.

For the elementary reaction results in this section, the descriptions contain the following, unless otherwise explicitly noted: comparisons of barriers and energetics include MCSCF ZPE; the CASSCF active spaces do not contain IOC and contain one lone O2p orbital in the MCSCF core; any reported MRMP2 barriers include all occurring reaction coordinate shifts; any reported CR-CC(2,3) barriers in the text do not include any shifts, are determined at the minima from the MCSCF IRC, and are listed with and without MCSCF ZPE; MR-AQCC barriers in the text always include MR-AQCC ZPE; any references made to stationary points refer to CASSCF stationary points (except for MR-AQCC optimizations); and individual pathways report only non-negligible geometry changes in CASSCF stationary points relative to Nguyen's [6] B3LYP and/or CASSCF results.

3.1 Triplet A′ pathway 1: $^{\cdot\cdot}O + C_2H_4 \rightarrow {}^{\cdot}CH_2CH_2O^{\cdot}$

This reaction has an A′ state in C_s symmetry throughout most of the pathway and is well represented by a (6,6) CAS. The reaction begins with an initial oxygen approach on the first excited state and then passes the A′ symmetric saddle point into the biradical region. Like the triplet A″ ground state pathway [1], this excited state path becomes asymmetric very close to the biradical minimum. The current methodologies of MCSCF usually do not allow for the determination of pure, asymmetric excited states. So, in order to obtain the IRC in this region, the calculations continued to use A′ symmetry and led to a symmetric stationary point that is not a minimum and contains a

Table 2 Barriers to reactions in kcal/mol calculated at the CAS level without and with (in parentheses) ZPE

Reaction pathway	CAS forward barrier[a]	CAS reverse barrier[a]	Nguyen forward barrier[b]	Nguyen reverse barrier[b]
Triplet A′ 1	19.8 (19.6)	17.4[c]	–	20.9
Singlet A_1 1	2.2 (2.5)	108.9 (104.8)	–	–
Singlet A″ 1	5.2 (5.2)	No C_s minimum	–	–
10	1.5 (1.0)	90.5 (86.6)	−2.9	82.0
11	0.2 (0.3)	59.8 (55.7)	1.6	59.1
12	6.8 (6.3)	80.0 (75.5)	0.0	74.2
13	95.0 (92.0)	64.8 (60.5)	86.3	58.9
M	17.1 (14.9)	ORF	–	–
20	95.0 (89.0)	66.6 (68.9)	81.3	55.6

Nguyen's barriers include ZPE

[a] CAS barriers are obtained from unconstrained optimizations unimolecular species and a distance of ∼3–5 Å for separated products

[b] Nguyen's barriers are the average barriers from several different levels of theory [6]

[c] This difference does not contain ZPE and is not a true barrier since it is taken from a C_s geometry that is not a minimum

single, imaginary frequency of -401 cm^{-1} that indicates that the OCCH dihedral angle bends out of the C_s plane. Also, including dynamic correlation leads to large changes in energetics and large shifts along the reaction coordinate. As a result, the forward barrier is 19.6 (3.3) kcal/mol at the CASSCF (MRMP2) level. This CAS barrier versus the MRMP2 barrier demonstrates the importance of dynamic correlation for this path. Other pathway discussions will not contain any further, unnecessary comparisons of CAS and MRMP2 barriers (see Tables 2 and 3).

Since the calculations could not fully determine the reverse barrier because of the symmetry-constrained IRC, the symmetric product provides an approximation. Given that the A″ geometries parallel the A′ geometries and the ground state A″ CASSCF ZPE changes the ground state reverse barrier by less than 1.0 kcal/mol [1], the excited state reverse barrier of 21.2 kcal/mol (without ZPE) at the MRMP2 level at the symmetric CASSCF stationary point nicely agrees with Nguyen's reverse barrier of 20.9 kcal/mol (with ZPE).

3.2 Singlet A_1 pathway 1: $^{\cdot\cdot}O + C_2H_4 \rightarrow$ oxirane

The calculations for this pathway used a (6,6) CAS with an A_1 state in C_{2v} symmetry throughout the IRC. Because numerical Hessian steps converge to different states in this case, Hessian calculations with a double zeta basis (which allows for analytic Hessian calculations in GAMESS) provided an approximate curvature for a triple zeta, saddle point search. Single-state MRMP2 leads to barrierless, oxygen addition for this excited state with an overall reaction exothermicity of -121.5 kcal/mol.

3.3 Singlet A″ pathway 1: $^{\cdot\cdot}O + C_2H_4 \rightarrow {}^{\cdot}CH_2CH_2O^{\cdot}$

A (6,6) CAS calculation was also used to study this pathway, which has an A″ state in C_s symmetry only throughout the forward barrier. The dihedral rotation breaks the symmetry near the $^{\cdot}CH_2CH_2O^{\cdot}$ biradical as discussed in the previous section. At the (6,6) CASSCF level of theory, the two lowest, singlet states appear to intersect one another near the forward barrier A″ saddle point, and again, problems with the numerical Hessian required a double zeta Hessian approximation. Including dynamic correlation results in a barrierless, overall energy change of -61.7 kcal/mol (without ZPE).

3.4 Pathway 10: $^{\cdot}CH_2CH_2O^{\cdot} \rightarrow CH_3CHO$

This pathway involves a H-atom shift and requires the use of a (14,14) CAS. It is one of several pathways with a TS (see Fig. 1) near the $^{\cdot}CH_2CH_2O^{\cdot}$ biradical and has several dominant determinants contributing to the wavefunction. The majority of path 10 is asymmetric with only acetaldehyde having an A′ state in C_s symmetry. While including some dynamic correlation does not lead to any substantial energy shifts along the reaction coordinate as shown in Fig. 2, it causes the forward barrier to change from a shallow height of 1.0 kcal/mol at the CASSCF level to a barrierless process. Therefore, no reverse barrier exists at the MRMP2 level along these CASSCF IRC points. The resultant barrierless reaction has an exothermicity of -77.6, -89.9, and -93.3 kcal/mol at the MRMP2, CR-CC(2,3), and CR-CC(2,3) without MSCF ZPE levels of theory, respectively. This energy difference shows the

Table 3 Barriers to reactions in kcal/mol calculated at the MRMP2 and CR-CC(2,3) levels with aug-cc-pVTZ basis

Reaction pathway	SPMRMP2[a]	Shifted MRMP2	MR-AQCC	Nguyen[b]/ Yang	Vertical MRMP2	Vertical MR-AQCC	Vertical CR-CC(2,3)
Triplet A′ 1 R	17.6[j]	21.2[j]	–	20.9	–	–	–
Triplet A′ 1 F	−0.8	2.8	–	–	−0.6	–	–
		3.3[c]					
Singlet A_1 1	−121.5	–	–	–	–	–	–
Singlet A″ 1	−61.7[d]	–	–	–	–	–	–
10	−77.6	–	–	−84.9	−81.0	–	−93.3
11 R	56.6	56.6	–	59.1	60.6	–	68.6
11 F	0.0	0.0	–	1.6	0.0	–	−0.3
		0.2[c]					
12 R	64.1	64.1	69.7[g,h]	74.2	67.0	74.6[h]	75.9
							73.5[i]
12 F	−3.4	−3.4	1.8[g,h]	0.0	−2.9	3.4[h]	−6.3
		0.4[c]					−4.4[i]
13 R	52.5	52.7	51.7[h]	58.9	56.9	55.8[h]	68.1
				53.9[e]			63.0[i]
13 F	78.3	78.5	83.0[h]	86.3	81.3	85.9[h]	94.2
				81.8[e]			90.8[i]
M R	ORF[f]	ORF[f]	–	–	ORF[f]	–	ORF[f]
M F	−1.6	−1.1	–	–	0.6	–	−6.7
		0.3[c]					
20 R	52.6	52.6	–	55.6	50.4	–	52.1
		52.8[c]					
20 F	76.7	76.8	–	81.3	82.8	–	87.4

The MR-AQCC barriers are calculated with the cc-pVDZ basis. F indicates the forward barrier, while R indicates the reverse barrier. Absence of F or R indicates reaction energies rather than barriers. The shifted MRMP2 barriers are formed based on the minima and maxima values of the MRMP2 single-point energies along the CASSCF IRC. Stationary point (SP) MRMP2 and shifted MRMP2 barriers include ZPE from CASSCF stationary points while MR-AQCC barriers derive from stationary points and ZPE at the MR-AQCC level. Nguyen's barriers include ZPE. Vertical MRMP2, vertical MR-AQCC, and vertical CR-CC(2,3) barriers do not include ZPE and are all at the same CASSCF geometries

[a] SPMRMP2 values derive from CAS stationary points, which are obtained from unconstrained optimizations of unimolecular species and a distance of ~3–5 Å for separated products

[b] Nguyen's barriers are the average barriers from several different levels of theory [6]

[c] MRMP2 barrier with ZPE from shifts in minima in addition to shifts in TSs

[d] Barrier does not include ZPE

[e] Yang's barriers at the CCSD(T)/cc-pVTZ//B3LYP/6-311++G* level of theory [14]

[f] ORF indicates orbital root flipping (see text for more complete description)

[g] This TS contains an extra imaginary frequency, which could not be eliminated for pathway 12 to retain an actual barrier

[h] Barrier is with cc-pVDZ basis

[i] Barrier is with aug-cc-pVDZ basis

[j] This difference does not contain ZPE and is not a true barrier since it is taken from a C_s geometry that is not a minimum

importance of including more dynamic correlation such as with CR-CC(2,3). It also indicates that other pathways (e.g., singlet A″ pathway 1) can contribute to path 10 products in a barrierless fashion if the $^{\cdot}CH_2CH_2O^{\cdot}$ biradical is in that particular pathway. This conclusion applies to any other pathways whereby dynamic correlation removes the reaction barrier.

During the hydrogen shift, the CCH angle of the action CH distance changes from 110° (CASSCF biradical) to 92° (CASSCF TS) in the forward barrier while the CO distance changes from 1.34 to 1.22 Å in the reverse barrier. Here and throughout this paper, "action" coordinates refer to internal coordinates that significantly change in length or degree relative to remaining (i.e., "non-action") internal coordinate changes, which are defined by cutoffs. Nguyen et al. [6] report geometries at the CASSCF(8,8)/cc-pVDZ level. All geometry differences between their study and this one remain negligible.

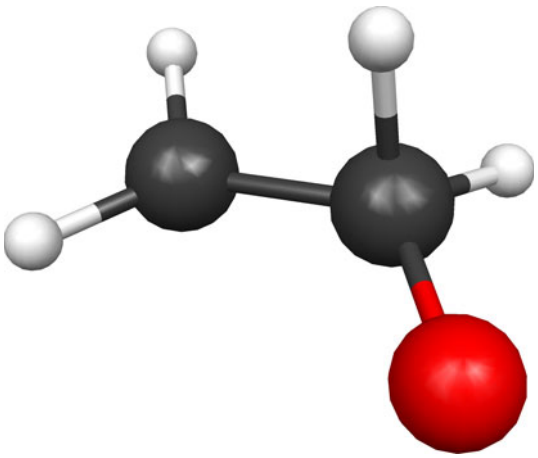

Fig. 1 TS geometry at the (14,14) CAS level of theory shown for pathway 10

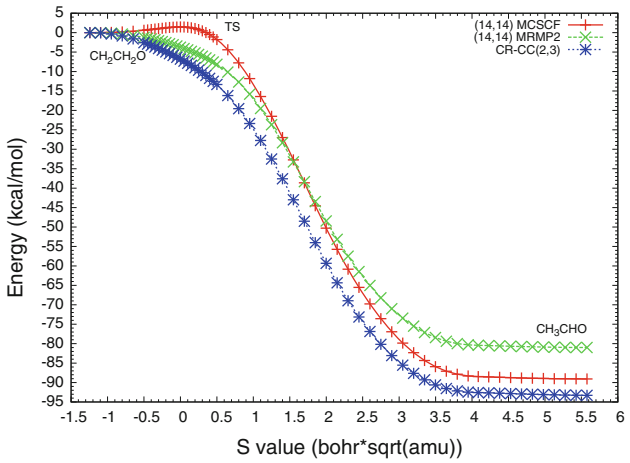

Fig. 2 (14,14) CAS IRC and MRMP2 single-point energies for pathway 10 shown with shifted energies so that the CAS energy equals the corresponding MRMP2 and CR-CC(2,3), single-point energies at the $^{\cdot}CH_2CH_2O^{\cdot}$ biradical. These results show how dynamic correlation leads to a barrierless reaction

3.5 Pathway 11: $^{\cdot}CH_2CH_2O^{\cdot}$ → oxirane

This pathway gives the ring closure of the $^{\cdot}CH_2CH_2O^{\cdot}$ biradical to oxirane and is well described by a (6,6) CAS. The CC distance changes by only ~0.03 Å across the entire reaction pathway in the (6,6) CAS, which includes the CC σ; thus, a (4,4) CAS could represent this reaction. However, since the initial part of this pathway requires SOC in the biradical region, a (6,6) CAS is appropriate and not much more expensive than a (4,4) CAS. This reaction has C_{2v} symmetry only for the oxirane minimum. Including dynamic correlation leads to results similar to the results for pathway 10. The reaction is essentially barrierless with a forward barrier of 0.2, −0.1, and −0.3 kcal/mol, whereas the reverse reaction has a barrier of 56.6, 64.5, and 68.6 kcal/mol at the MRMP2, CR-CC(2,3), and CR-CC(2,3) without MCSCF ZPE levels, respectively.

With several determinants contributing to the wavefunction, this TS also has biradical character and geometrically resembles the starting biradical, $^{\cdot}CH_2CH_2O^{\cdot}$. Both the biradical minimum and TS geometries have a CO (CC) distance of 1.41 (1.51) Å. The OCC angle is 116° in the minimum structure and 115° in the TS, and the smaller OCCH dihedrals for both structures are 14 ± 1°. However, the OCCH dihedral for the minimum is 176° and for the TS is 148°. Oxirane has a CO distance of 1.44 Å, a CC distance of 1.48 Å, and a COC angle of 62°. In this study, both dihedral angles in the TS geometry significantly differ from Nguyen et al. [6] B3LYP (CASSCF) values of 37° (26°) and 130° (129°) for the TS. As will be shown in the surface crossings section, this (6,6) CAS consistently recovers correlation in the biradical region as opposed to an (8,8) CAS with IOC. This factor strongly affects the accuracy of the forward barrier. Indeed, these structural differences emphasize the need for careful determination of the proper CAS sizes for this very complex region close to the $^{\cdot}CH_2CH_2O^{\cdot}$ biradical.

3.6 Pathway 12: $^{\cdot}CH_2CH_2O^{\cdot}$ → CH_2CHOH

With a (10,10) CAS, this pathway is dominated by a hydrogen shift. The majority of this pathway does not have symmetry; vinyl alcohol has C_s symmetry. At the MRMP2 level, this reaction is almost barrierless with a forward barrier of 0.4 kcal/mol. Hence, this pathway represents the third reaction to originate from $^{\cdot}CH_2CH_2O^{\cdot}$ and to become barrierless with application of MRMP2, single-point energies. Furthermore, the shifted, CR-CC(2,3) energies for the forward barrier are also small at 0.7 kcal/mol. However, unlike pathways 10 and 11, the MRMP2 and CR-CC(2,3) single-point energies along the CASSCF IRC for pathway 12 still have some curvature that resembles the CASSCF IRC near the TS instead of appearing totally barrierless (see path 10, 11, and 12 IRC plots in the Supporting Information). The reverse barriers are 64.1, 71.4, and 75.9 kcal/mol at the MRMP2, CR-CC(2,3), and CR-CC(2,3) without MCSCF ZPE levels, respectively. At the MR-AQCC level, the forward barrier is 1.8 kcal/mol, while the reverse barrier is 69.7 kcal/mol. However, for this theory level, the TS displays a first imaginary frequency of $-1241\ cm^{-1}$ and a second imaginary frequency of $-91\ cm^{-1}$ that could not be eliminated.

Given both discrepancies among the various levels of theory and computational limitations, single-point energies using first- and second-order CI (CISD) with Davidson +Q correction[55, 56] from a (4,4) CAS (MR-CI + Q) and aug-cc-pVDZ basis, both with and without additional excitations out of the core non-1 s orbitals, were performed

on the forward barrier via the occupation restricted multiple active space (ORMAS) [57] implementation in GAMESS. At the same geometries, CR-CC(2,3) calculations were also performed with the aug-cc-pVDZ basis for comparison purposes. Without ZPE, these single-point energy results give forward barriers of 1.7, 9.8, −1.0, and 9.8 kcal/mol for MR-CI, MR-CI without the additional excitations, MR-CI + Q, and MR-CI + Q without the additional excitations, respectively, and −4.4 (−6.3) kcal/mol for CR-CC(2,3) with the aug-cc-pVDZ (aug-cc-pVTZ) basis. Combined with additional single-point energies at these geometries (Table 3) and the above discussion for path 12, these results strongly support that the forward barrier is in fact barrierless.

The biradical character of the TS causes it to mostly resemble the initial, $^{\cdot}CH_2CH_2O^{\cdot}$ biradical. As the reaction progresses from the biradical to the TS, the action HCO angle changes from 104° to 74°, and the non-action HCCH dihedral changes from 60° to 21°. The CC distance changes from 1.51 to 1.35 Å during the course of the full reaction.

3.7 Pathway 13: $CH_3CHO \rightarrow$ oxirane

This portion of the PES is very difficult to characterize given that the concerted hydrogen shift with CO bond formation most likely involves several asymmetric, quasi-degenerate states. In more general terms, this pathway requires not only a transformation among lone pair and bond–antibond orbitals but also a change in dominant configurations over a small range of nuclear geometries. Because of the extremely flat, MEP curvature around the biradical-like TS, locating this stationary point proved difficult in calculations both with and without analytic Hessians. Several CAS sizes show one imaginary frequency after geometry optimization. However, depending on the initial geometry, active spaces without either the O2p or the CC σ, σ^* orbitals can lead to a TS with a reasonable, distinct, single imaginary frequency that does not lead to acetaldehyde via a traditional IRC. Instead, the IRC calculations led to path 11 stationary points (sometimes with convergence issues far into the IRC calculation). Hence, even though such configuration expansions result in the proper curvature for the TS, they do not necessarily give the desired IRC (e.g., pathway 13).

This path must have at least a (16,16) CAS in order to include all quasi-degenerate effects. Since a (16,16) CAS is very computationally expensive, a (10,10) CAS with the non-action CH orbitals in the core provides a compromised solution. Because this path is so difficult to follow, GVB-PP calculations provided an initial TS geometry with the CH_2 torsion dominating the imaginary frequency. The resulting (10,10) CAS IRC gives the correct reaction endpoints. Since the (10,10) CAS is a compromise, another (12,12) CAS was examined to provide a comparison for the energetics. The MCSCF core of the (12,12) CAS contains the O2 s, CC σ, and the lone O2p orbitals in addition to the chemical core orbitals and produced stationary point energetics comparable to those obtained with the (10,10) CAS. However, this (12,12) CAS gives incorrect IRC endpoints. At the SPMRMP2 level, the forward (reverse) barrier is 78.3 (52.5) kcal/mol for the (10,10) CAS and 79.3 (51.1) kcal/mol for the (12,12) CAS. The CR-CC(2,3) (CR-CC(2,3) without MCSCF ZPE) calculations resulted in a forward barrier of 91.2 (94.2) kcal/mol and a reverse barrier of 63.8 (68.1) kcal/mol. Based on the MRMP2 and CR-CC(2,3) results, dynamic correlation changes the barrier heights but does not result in any horizontal shift in the location of the TS. At the MR-AQCC level, the forward barrier is 83.1 kcal/mol, while the reverse barrier is 51.7 kcal/mol. Also, at this theory level, a Hessian calculation on TS 13 produced a $-535\ cm^{-1}$ imaginary frequency with the same qualitative nature as the corresponding GVB-PP and CAS imaginary frequencies.

TS 13 lies along a particularly flat region of the potential; this characteristic flatness distinctly shows up in the IRC. In addition, MRMP2 (MR-AQCC) energies with the aug-cc-pVTZ (cc-pVDZ) basis give an overall reaction enthalpy of 25.8 (31.2) kcal/mol, which compares well to an experimental enthalpy of 27.1 kcal/mol [58–60].

Multiple geometrical changes occur for this reaction. In particular, this TS resembles the TSs for paths 10–12 and also has several dominant configurations contributing to the wavefunction. For the TS, only slight differences between this study and Nguyen's study exist for the two HCC angles for the hydrogens closest to the oxygen.

3.8 Pathway Miyoshi M and 20: $^{\cdot}CH_2CH_2O^{\cdot} \rightarrow CH_2CO + H_2$ and $CH_3CHO \rightarrow CH_2CO + H_2$

As shown above, representations of the pathways through the biradical region strongly depend on the CAS size. For the multiple bond changes in this pathway, inclusion of the O2p orbital in the active space or not determines what path, that is, M or 20, actually exists for the given level of theory. At the (10,10) CAS level, putting the O2p orbital in the MCSCF core leads to path M with a symmetric, A′ TS. Starting from this TS geometry and placing the O2p in the active space for a (12,11) or (12,12) CAS leads to an asymmetric TS that leads to path 20 from Nguyen et al. [6] rather than path M.

The complexity with active space continues when examining the IRCs. For pathway M with the (10,10) CAS, ORF occurs toward the end of the IRC for the products. This ORF occurs during CO π bond formation, which should be obvious given the product geometries. Thus,

since a CAS with the O2p is required for the products and does not give the TS for pathway M, the reverse barrier is unavailable at the MRMP2 level, and since there is no viable IRC, the CR-CC(2,3) barrier is also not reported. With the (10,10) CAS at the MRMP2 level, the forward barrier is 0.3 kcal/mol. Shifted CR-CC(2,3) values give the forward barrier as −2.7 kcal/mol.

Pathway 20 is found by either a (12,11) or (12,12) CAS and is the dissociation of a hydrogen molecule from acetaldehyde. It is the second of the pathways in the series of compromised active spaces due to computational expense, with pathway 13 being the first. To fully describe all of these compromised pathways requires at least a (16,15) or (16,16) CAS if no ORF occurs. For pathway 20, the compromised (12,12) CAS comes from taking acetaldehyde's methyl group and placing two of the three initially degenerate CH σs in the core. For the IRC leading to acetaldehyde using a compromised CAS, the active CH σ, σ^* orbitals do not lie in the plane of symmetry. As well, when the IRC reaches the $H_2CCO + H_2$ products separated by $\sim$4 Å, the bimolecular product does not fully separate, and H_2 does not lie in the symmetry plane of the H_2CCO molecule. Therefore, symmetry was not used in these calculations. Also, this particular pathway forms another CO π, π^* and thus has IOC for the $H_2CCO + H_2 \sim 4$ Å product. The single-point MRMP2 shifts the minima along the reaction coordinate very little, and the forward barrier (reverse barrier) is 76.8 (52.8) kcal/mol at the MRMP2 level. The experimental reaction enthalpy is 27.8 kcal/mol [58, 60–63], which lies within 4 kcal/mol of the MRMP2 enthalpy. The CR-CC(2,3) (CR-CC(2,3) without MCSCF ZPE) level results in a forward barrier of 81.4 (54.4) kcal/mol, a reverse barrier of 87.4 (52.1) kcal/mol, and an overall enthalpy of 27.0 kcal/mol, which lies within 1 kcal/mol of the experimental enthalpy.

For path 20 in the forward barrier, the HH distance goes from 2.58 to 1.03 Å, while for the reverse barrier, it changes from 1.03 to 0.76 Å. The methyl group CH distance changes from 1.11 to 1.68 Å for the forward barrier. The CC distances are 1.53, 1.42, and 1.33 Å at the stationary points in this pathway. This study's TS has only a slight difference from Nguyen's TS; the departing hydrogen from the terminal carbon lies 1.51 (1.38) Å from the carbon nearest the oxygen in this (Nguyen's) study. (The Supporting Information contains plots of both paths M and 20.)

3.9 Geometry comparisons between the $^{\cdot}CH_2CH_2O^{\cdot}$ biradical and TSs 10–13

Despite the different active spaces, TSs 10–13 display several geometrical similarities. The smallest, OCCH dihedral angle ranges from 10° to 24° and the OCC angle ranges from 115° to 125°. The CO distance varies from 1.34 to 1.41 Å, and the CC distance has a range of 1.43 to 1.51 Å. For the non-action Hs closest to the O, the two OCH angles cannot be distinguished. Likewise, for the Hs farthest from the O, the OCH angles also show no substantial differences (e.g., range from 116° to 120°). Indeed, besides slight differences in the action areas that differentiate key features of the reactions themselves, these four TSs appear almost identical. Furthermore, these TS geometries from paths 10–12 differ little from the $^{\cdot}CH_2CH_2O^{\cdot}$ biradical geometries obtained with the various CAS spaces: the CO distances differ by less than 1.00 Å, the CC distances also differ by less than 1.00 Å, and the OCCH dihedral (OCC angle) differs by 18° (9°) at most.

3.10 Surface crossings at the MCSCF level: $^{\cdot}CH_2CH_2O^{\cdot}$ and $^{\cdot}CH_2CHOH$

This study found two relevant surface crossings—one near the $^{\cdot}CH_2CH_2O^{\cdot}$ biradical and one near the $^{\cdot}CH_2CHOH$ biradical. GAMESS currently cannot use MRMP2 for the MEX search because the MEX search requires analytic gradients, so MCSCF wavefunctions are used in these MEX calculations. Therefore, it is important to find an active space that gives consistent results with expected correlation effects. In order to justify the active space choice for a MEX of interest, Table 4 shows CAS and MRMP2 singlet–triplet energy gaps at $^{\cdot}CH_2CH_2O^{\cdot}$ for the (6,6) and (8,8) CAS pure electronic states. The (6,6) CAS for the MEX and path 1 are the same. These singlet–triplet gaps show how increasing the active space by adding the lone O2p leads to inconsistent correlation recovery in the MRMP2 results relative to the CASSCF results; that is, single-state MRMP2 fails when the active space leads to quasi-degenerate electronic states (this perturbative, single-state root flipping is well known [22]).

The $^{\cdot}CH_2CH_2O^{\cdot} \rightarrow {}^{\cdot}CH_2CHOH$ reaction on the triplet surface (i.e., pathway 6 from our first study [1]) contains both crossings. The $^{\cdot}CH_2CH_2O^{\cdot}$ MEX geometry has a CO distance of 1.43 Å and a small OCCH dihedral of 61°, whereas the $^{\cdot}CH_2CHOH$ MEX occurs at a CO distance of 1.40 Å and a small OCCH dihedral of 67°. Paths 1 and 6

Table 4 (6,6) and (8,8) CAS and MRMP2 triplet–singlet gaps in kcal/mol at the $^{\cdot}CH_2CH_2O^{\cdot}$ biradical triplet minimum

Triplet–singlet gap (kcal/mol)	(6,6) Triplet minimum geometry	(8,8) Triplet minimum geometry
(6,6) CAS	0.6	0.8
(6,6) MRMP2	0.7	0.9
(8,8) CAS	0.4	1.3
(8,8) MRMP2	−0.4	0.5

SOC results and further investigation into the $^{\cdot}CH_2CH_2O^{\cdot}$ biradical give better insight into the PES near these MEXs.

3.11 SOC single-point energies: $^{\cdot\cdot}O + C_2H_4 \rightarrow {}^{\cdot}CH_2CH_2O^{\cdot}$

To further understand the multiple, close-lying PESs in the reaction, additional calculations were performed along the IRC for path 1. As previously discussed, since a pure state (8,7) CAS has convergence difficulties for path 1, CASSCF optimizations were done with a (6,6) CAS. However, the (6,6) CAS does not allow for simultaneous exploration of all close-lying states. The (8,7) SA CAS contains the lone O2p orbital, which essentially allows for the important configurations necessary for two of the four quasi-degenerate states near $^{\cdot}CH_2CH_2O^{\cdot}$. As discussed in the methods section, (8,7) SA CAS, single-point energies followed by SO-MCQDPT2, single-point energies should give the quasi-degenerate states and perturbatively recover the dynamic correlation and SOC effects from those several close-lying states.

Calculations using the (8,8) SA CAS, MCQDPT2 method were also performed for the biradical region to see whether it would be an effective CAS size. It was found that the (8,8) SA CAS configurations qualitatively differ from the (8,8) MCQDPT2 configurations, whereas configurations between the (8,7) SA CAS and (8,7) MCQDPT2 do not qualitatively differ. In other words, for the (8,8) SA CAS, the dominant configurations drastically change with the perturbation. Thus, this study uses an (8,7) SA CAS reference to further examine path 1 as well as the $^{\cdot}CH_2CH_2O^{\cdot}$ biradical region rather than an (8,8) CAS.

For pathway 1, the nonrelativistic, triplet A″ IRC from the O + ethylene to the $^{\cdot}CH_2CH_2O^{\cdot}$ biradical has the nonrelativistic, triplet A′ state lying very close throughout the path. To obtain the relativistic potentials, (8,7) SA CAS, single-point energies followed by SO-MCQDPT2, single-point energies were calculated at the (6,6) CAS IRC geometries. However, for the SA CAS, only careful state selection yields physically reasonable, smooth curves. Using an (8,7) SA CAS with the three lowest-lying, nonrelativistic triplets gives a reasonable wavefunction for obtaining SOC results—nine relativistic triplets and five relativistic singlets—until near the triplet A″ TS (see Figs. 3, 4, 5). Since SO-MCQDPT2 and SO-CASCI coupling constants are in good agreement, only the latter are given.

The three nonrelativistic triplets no longer remain degenerate near the $^{\cdot}CH_2CH_2O^{\cdot}$ biradical. One of these surfaces becomes much higher in energy and prevents correct results with MCQDPT2 in that surface region (see Supporting Information for the additional graphs). Because of this limitation, additional calculations were repeated

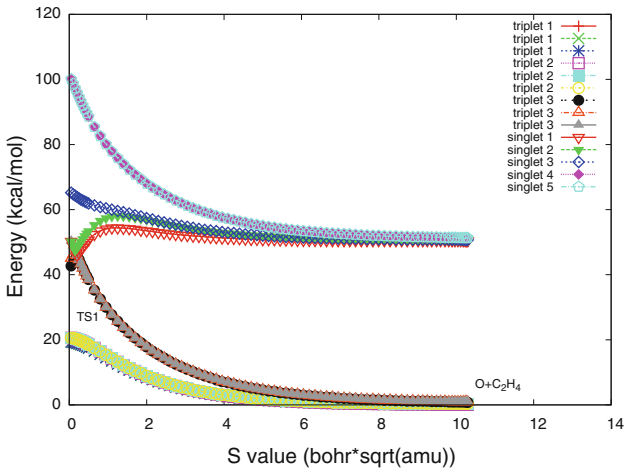

Fig. 3 Path 1 SO-CASCI single-point energies shown with nine triplets and five singlets from an (8,7) SA CAS on the three lowest-lying, nonrelativistic triplets. Here, the following pairs of relativistic state energies almost always overlap: singlets 4 and 5, and the upper 3 triplets

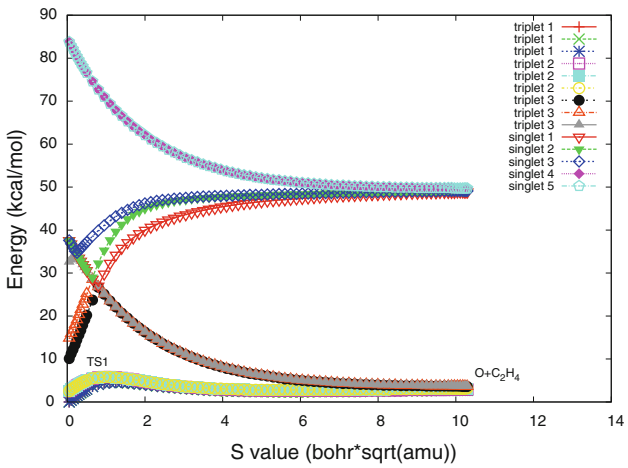

Fig. 4 Path 1 SO-MCQDPT2 single-point energies shown with nine triplets and five singlets from an (8,7) SA CAS on the three lowest-lying, nonrelativistic triplets. Here, the following pairs of relativistic state energies almost always overlap: singlets 4 and 5, and the upper 3 triplets

with an (8,7) SA CAS using the two lowest-lying, nonrelativistic triplets and the two lowest-lying, nonrelativistic singlets in order to obtain SOC results across the entire IRC for path 1. Figures 6, 7, 8 display the results from the TS to $^{\cdot}CH_2CH_2O^{\cdot}$. In particular, Fig. 8 shows a sharp but continuous change in the coupling constants; this change corresponds to the OCCH dihedral rotation at the end of path 1. Thus, these four states (two triplets and two singlets) will prove very important in determining any dynamics for this system.

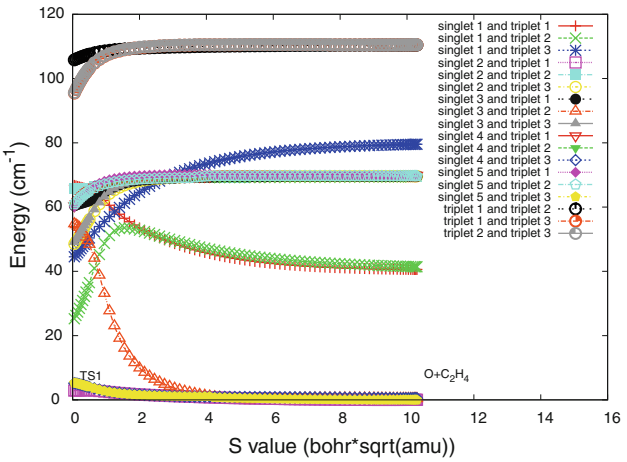

Fig. 5 Path 1 SO-CASCI single-point coupling constants shown with nine triplets and five singlets from an (8,7) SA CAS on the three lowest-lying, nonrelativistic triplets. Here, the following set of coupling constants almost always overlap: triplets 1 and 3 with triplets 2 and 3; singlet 4 and triplet 1 with singlet 5 and triplet 2; and singlet 2 and triplet 1, singlet 4 and triplet 3, and singlet 5 and triplet 3

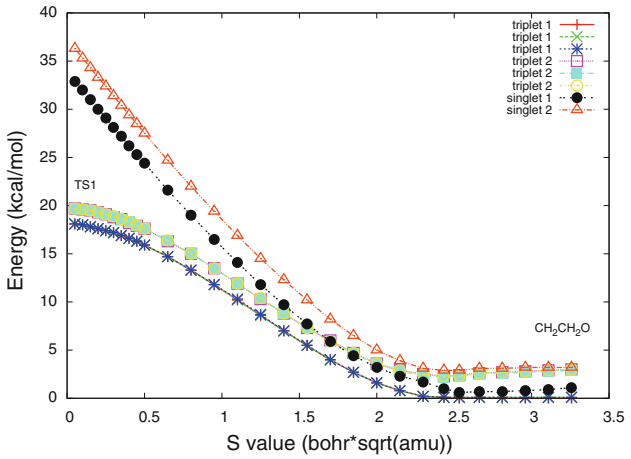

Fig. 6 Path 1 SO-CASCI single-point energies shown with six triplets and two singlets from an (8,7) SA CAS on the two lowest-lying, nonrelativistic triplets and two lowest-lying, nonrelativistic singlets. Here, the following relativistic state energies almost always overlap: the first 3 triplets, and the second 3 triplets

3.12 SOC single-point energies: $^{\cdot}CH_2CH_2O^{\cdot} \rightarrow {}^{\cdot}CH_2CHOH$

Pathway 6 on the lowest-lying triplet surface has quasi-degeneracy with several surfaces. In this case, four states lie near the $^{\cdot}CH_2CH_2O^{\cdot}$ biradical, but only a triplet and singlet lie close between the TS and $^{\cdot}CH_2CHOH$. Using the (8,8) CAS IRC geometries, several SA CAS wavefunctions were examined to give more information on the close-lying states for this part of the PES. For example, a (10,9) SA CAS would be appropriate to describe all four states. However, ORF does not allow the SA CAS to be consistent

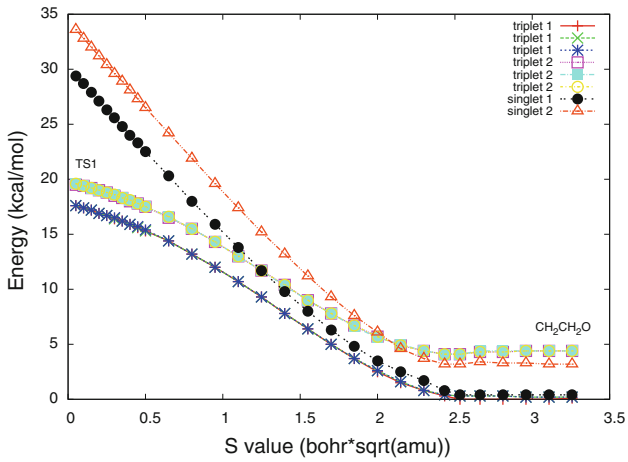

Fig. 7 Path 1 SO-MCQDPT2 single-point energies shown with six triplets and two singlets from an (8,7) SA CAS on the two lowest-lying, nonrelativistic triplets and two lowest-lying, nonrelativistic singlets. Here, the following relativistic state energies almost always overlap: the first 3 triplets, and the second 3 triplets

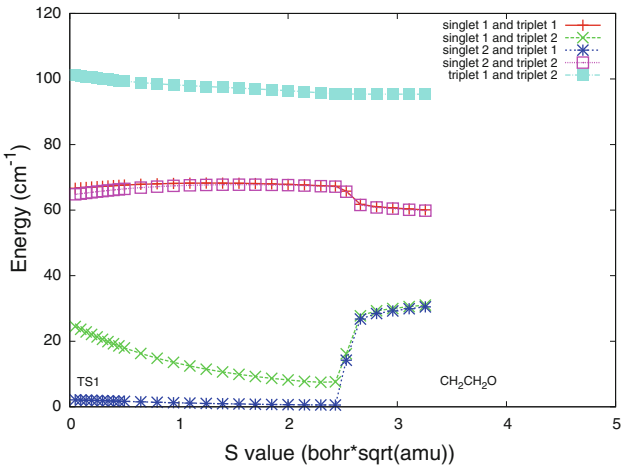

Fig. 8 Path 1 SO-CASCI single-point, coupling constants shown with six triplets and two singlets from an (8,7) SA CAS on the two lowest-lying, nonrelativistic triplets and two lowest-lying, nonrelativistic singlets

at all geometries: the O2p* IOC orbital displaces the relevant CH σ* orbital despite various attempts to maintain the active space. Therefore, an (8,8) SA CAS is used to obtain accurate SOC results for the lowest-lying triplet and close-lying singlet for the full path as compared to the lowest state results from the (10,9) SA CAS on the $^{\cdot}CH_2CH_2O^{\cdot}$ biradical half of the path. Figure 9 shows the energetics for this hydrogen migration at the (8,8) SO-CASCI level. All coupling constants along this path are less than 4 cm^{-1}. These SOC constants do not match the (10,9) CAS couplings near $^{\cdot}CH_2CH_2O^{\cdot}$ since the (8,8) CAS does not contain some states of interest due to its lack of the O2p in the active space.

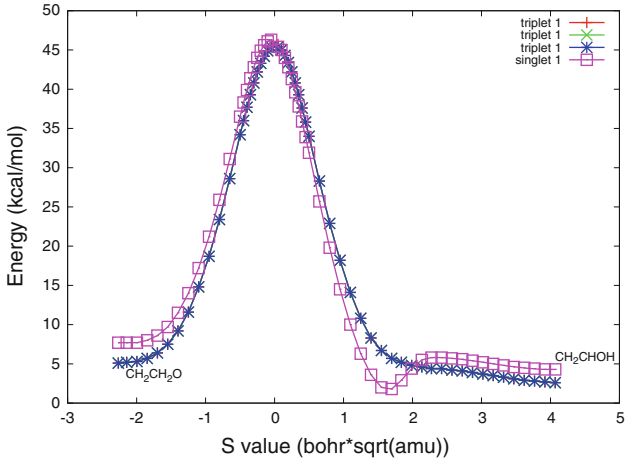

Fig. 9 Path 6 SO-CASCI single-point energies shown with three relativistic triplets and one singlet from an (8,8) CAS that is SA with the lowest-lying, nonrelativistic triplet and lowest-lying, nonrelativistic singlet. Here, the three relativistic triplet curves are indistinguishable because of overlap in the energies

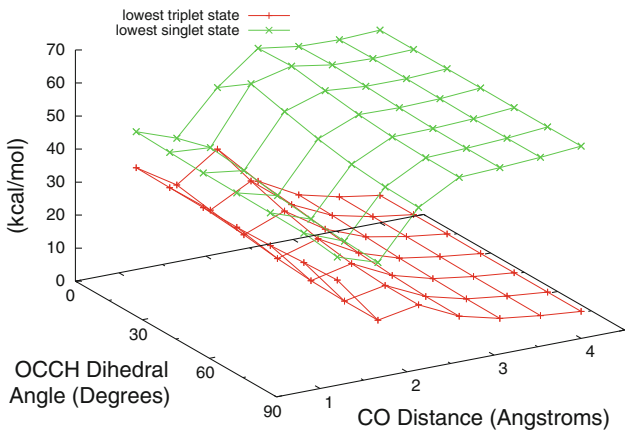

Fig. 10 (6,6) CAS triplet constrained optimizations and (6,6) CAS singlet single-point energies on a large region of PES for overview energetics

3.13 SOC single-point energies around the $^{\cdot}CH_2CH_2O^{\cdot}$ biradical

With several singlet TSs in this PES region (TS 10–13) and several close-lying surfaces, a finer description of the $^{\cdot}CH_2CH_2O^{\cdot}$ biradical region of the PES requires two nonrelativistic singlet and two nonrelativistic triplet states. Path 1 leads to large changes in the OCCH dihedral near the $^{\cdot}CH_2CH_2O^{\cdot}$ biradical. Thus, in order to describe these lower state curvatures over an extended geometry range, (6,6) CAS triplet constrained optimizations and (6,6) CAS singlet single-point energies were performed on a grid from 1.2 to 4 Å for the CO distance and from 0 to 90° for the OCCH dihedral in increments of 0.5 Å and 15°, respectively. The boundary of 1.2 Å was chosen since ORF occurs toward the more repulsive part of the potential.

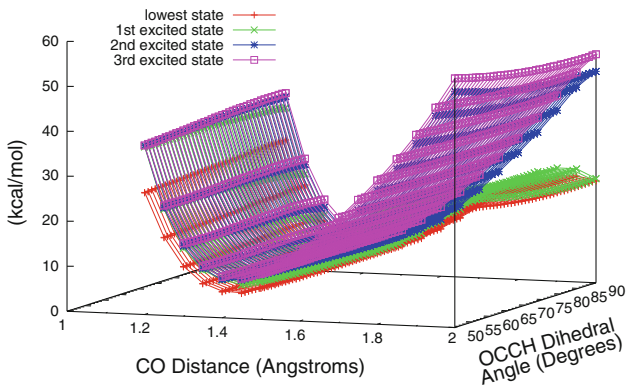

Fig. 11 (8,7) SA CAS single-point energies for 4 lowest-lying states—two singlets and two triplets—on top of (6,6) CAS triplet constrained optimizations about the $^{\cdot}CH_2CH_2O^{\cdot}$ biradical

Figure 10 shows this region of the PES from these calculations. A crude outline of the MEP of path 1 can be seen along the 90° dihedral. As the initial oxygen approach reaches an OCCH dihedral angle of 0°, the constrained optimizations no longer lead to the biradical but to the initial minimum for hydrogen abstraction from ethylene.

In order to refine the results in the quasi-degenerate PES region, the same calculations were performed as above, but with a narrower range of geometries and a finer resolution; that is, for 1.2–2 Å and 50–90° in increments of 0.05 Å and 1°, respectively. Then, (8,7) SA CAS (see Fig. 11) and SOC calculations were performed on the four lowest-lying states as described above. As shown in Fig. 11, these lowest-lying states are nearly degenerate at many points around the biradical region. Figures 12,13 give the CASCI and MCQDPT2 contours of the lowest-lying, nonrelativistic singlet relative to the lowest-lying, nonrelativistic

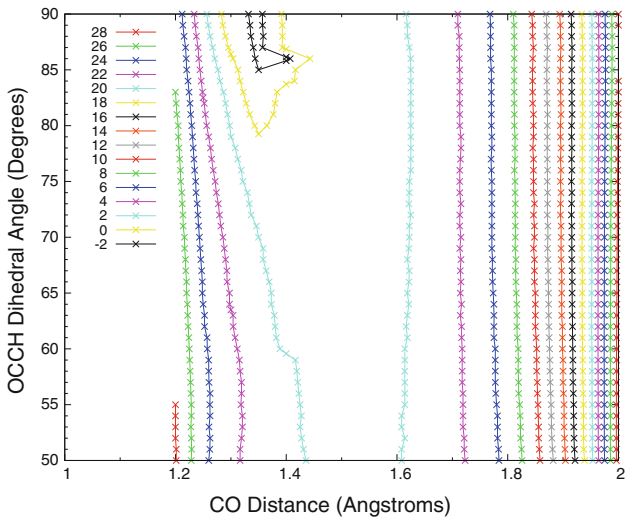

Fig. 12 CASCI single-point energies from an (8,7) SA CAS in kcal/mol for lowest-lying, singlet–triplet gap about the $^{\cdot}CH_2CH_2O^{\cdot}$ biradical

triplet. Figure 14 displays the SOC coupling constants for the lowest-lying, singlet–triplet gap in this region (the Supporting Information contains excited state plots of this region). In particular, this figure shows that the relativistic energy changes as the OCCH dihedral rotates. The coupling constants vary in a "half cone-like" fashion with respect to the OCCH dihedral angle near ~1.4 Å CO distance and ~60° OCCH dihedral—coordinates near the (6,6) CAS, $^{\cdot}CH_2CH_2O^{\cdot}$ MEX. It is expected that this PES region will strongly influence the non-adiabatic dynamics as a result of the many quasi-degenerate states, showing that a single-state, single-reference approach may miss much of the essential non-adiabaticity.

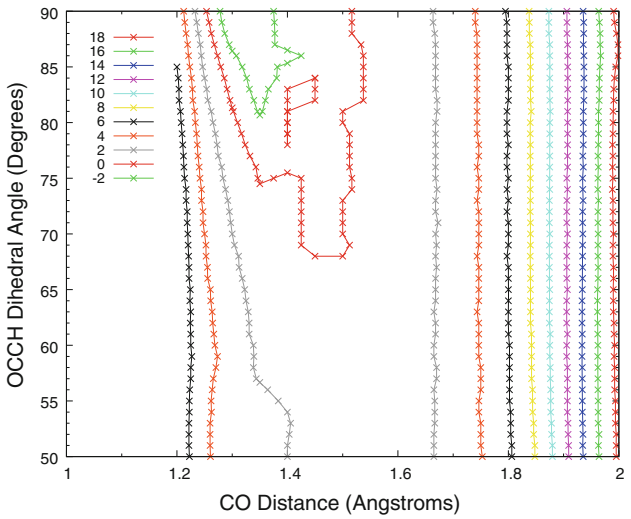

Fig. 13 MCQDPT2 single-point energies from an (8,7) SA CAS in kcal/mol for lowest-lying, singlet–triplet gap about the $^{\cdot}CH_2CH_2O^{\cdot}$ biradical

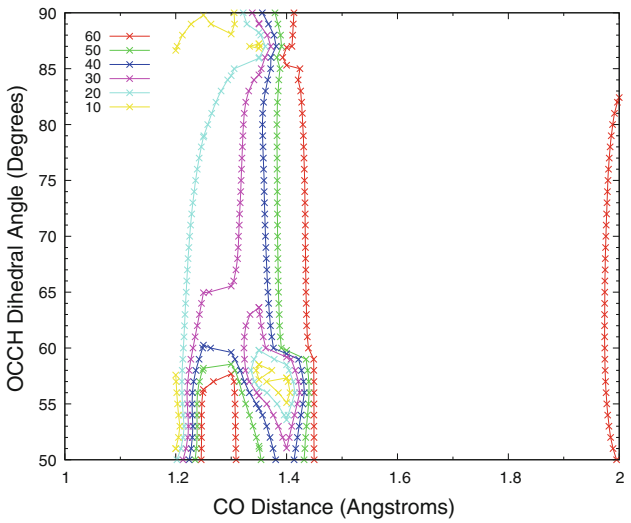

Fig. 14 SO-CASCI single-point coupling constants from an (8,7) SA CAS in cm^{-1} for lowest-lying, singlet–triplet gap about the $^{\cdot}CH_2CH_2O^{\cdot}$ biradical

4 Conclusions

In this work with careful choice of the active space, CASSCF, MRMP2, MR-CISD, and MR-AQCC are used to model the multiconfigurational nature of the singlet surface for the addition of oxygen atom to ethylene. Reaction paths involving the biradical region (paths 1 and 10–13) clearly have many configurations contributing to the wavefunction and thus require a multiconfigurational treatment to account for non-dynamical correlation. In particular, with pure state solutions, TSs 10–13 all have similar geometries with MEPs in a very flat PES region. Relative to available data from single-reference treatments, multireference calculations resulted in the following significant differences for TS geometries in this region: (1) for path 13, the CO distance with the (10,10) CAS results in 1.40 Å while Nguyen's [6] B3LYP yields 1.31 Å, and (2) for path 20 for one action CH distance, (12,12) CAS shows 1.51 Å, whereas Nguyen's [6] B3LYP gives 1.38 Å.

While perturbative, dynamic correlation does not have much effect on the geometries of the singlet stationary points, dynamic correlation is *essential* for obtaining reasonable energetics. Although the MRMP2 captures a significant portion of the dynamic correlation, this treatment certainly does not encapsulate all of it. While multiple levels of theory have been used in this study, the best level of theory for barrier energetics is still not well understood. Since the biradical regions clearly require multiconfigurational wavefunctions, it is anticipated that CR-CC(2,3) barriers may require more non-dynamical correlation while the MRMP2 barriers require more dynamic correlation. The MR-AQCC calculations hold promise, but are limited to smaller basis sets and active spaces because of the computational expense. CR-CC(2,3) gives values within 1 kcal/mol of the experimental values for the thermodynamics of pathways 13 and 20, while MRMP2 is within 1.5 kcal/mol for pathway 13 and within about 4.0 kcal/mol for pathway 20. Computational expense limits the latter pathway to a compromised CAS, which may explain a significant part of this error. However, these comparisons with experiment are for closed shell molecules and do not help to elucidate the best methods for obtaining energetics in the biradical regions.

At the MRMP2 and CR-CC(2,3) levels, pathways 1, 10, 11, 12, and M are essentially barrierless processes, which again emphasizes the need for a careful treatment of this part of the PES. Furthermore, in paths 13 and M, the addition of O2p to the active space qualitatively changes these pathways at the CASSCF level in the sense that a geometrically similar TS leads to different minima. However, whenever possible, CASSCF active spaces for pure states do not contain lone O2p orbitals, which tend to lead to IOC ORF with the current, convergence techniques. This

active space construction is particularly important in both solving for pure states at the CASSCF level (avoiding IOC ORF) and obtaining single-state MRMP2 results (avoiding state root flipping).

In addition to the pure state calculations of the reactions, this study explicitly and appropriately examines the biradical regions. First, two separate CASSCF surface crossings between the lowest-lying triplets and lowest-lying singlets are determined. Second, an (8,7) SA CAS is used to describe the $^{\cdot}CH_2CH_2O^{\cdot}$ biradical around this CASSCF approximation to the given surface crossing. Third, SO-MCQDPT2 is performed on the lowest four states in a region around $^{\cdot}CH_2CH_2O^{\cdot}$. Without treatments such as non-orthogonal MCSCF, these quasi-degenerate states currently require SA wavefunctions to sort out close-lying states—with or without IOC. This active space selection requires care since MCQDPT2 application to an (8,8) SA CAS reference changes the dominant configuration(s). This fact also supports the avoidance of improper IOC in SA MCSCF, reference wavefunctions.

Overall, the O + ethylene PES definitely requires a complex treatment in the quasi-degenerate regions around the MEXs. In fact, PES regions about paths 10–13 will need more sophisticated, multireference methods incorporating dynamic correlation in order to develop an accurate potential for dynamic simulations. Future work on O + ethylene will take a number of directions that include further GVB-PP and MR-AQCC energetics, various coupled cluster calculations, and dynamical simulations including but not limited to surface hopping.

Acknowledgments The authors are indebted to Michael W. Schmidt and Mark S. Gordon for help in using the capabilities of GAMESS and MCSCF. This material is based upon work supported by the National Science Foundation under Grant No. OISE-0730114 for the Partnerships in International Research and Education (PIRE) and by the Robert A. Welch Foundation under Grant No. D-0005. TeraGrid resources were provided by the Texas Advanced Computing Center (TACC). Support was also provided by the High-Performance Computing Center (HPCC) at Texas Tech University, under the direction of Philip W. Smith. In addition, this work was supported by the Austrian Science Fund within the framework of the Special Research Program F16 (Advanced Light Sources) and Project P18411-N19. Computer time at the Vienna Scientific Cluster (project no. 70019) is gratefully acknowledged. TLW acknowledges computing resources purchased through funds provided by Ames Laboratory and Iowa State University.

References

1. West AC, Kretchmer JS, Sellner B, Park K, Hase WL, Lischka H, Windus TL (2009) O(3P) + C2H4 potential energy surface: study at the multi reference level. J Phys Chem A 113(45):12663
2. Gardiner WC Jr (ed) (1984) Combustion chemistry. Springer, New York
3. Casavecchia P, Capozza G, Segoloni E, Leonori F, Balucani N, Volpi Gian G (2005) Dynamics of the O(3P) + C2H4 reaction: identification of five primary product channels (vinoxy, acetyl, methyl, methylene, and ketene) and branching ratios by the crossed molecular beam technique with soft electron ionization. J Phys Chem A 109(16):3527
4. Su H, Zhao S, Liu K, Xiang T (2007) The reactions of O(3P) with terminal alkenes: the H2CO channel via 3,2 H-atom shift. J Phys Chem A 111(38):9600
5. Lee S-H, Huang W-J, Chen W-K (2007) Dynamics of the reaction of atomic oxygen with ethene: observation of all carbon-containing products by single-photon ionization. Chem Phys Lett 446(4–6):276
6. Nguyen TL, Vereecken L, Hou XJ, Nguyen MT, Peeters J (2005) Potential energy surfaces, product distributions and thermal rate coefficients of the reaction of O(3P) with C2H4(X1Ag): a comprehensive theoretical study. J Phys Chem A 109(33):7489
7. Yamaguchi K, Yabushita S, Fueno T, Kato S, Morokuma K (1980) Geometry optimization of the ring-opened oxirane diradical: mechanism of the addition reaction of the triplet oxygen atom to olefins. Chem Phys Lett 70(1):27
8. Dupuis M, Wendoloski JJ, Takada T, Lester WA Jr (1982) Theoretical study of electrophilic addition: atomic oxygen(3P) + ethylene. J Chem Phys 76(1):481
9. Fueno T, Takahara Y, Yamaguchi K (1990) Approximately projected UHF Moeller-Plesset calculations of the potential energy profiles for the reaction of the triplet oxygen atom with ethylene. Chem Phys Lett 167(4):291
10. Smith BJ, Nguyen Minh T, Bouma WJ, Radom L (1991) Unimolecular rearrangements connecting hydroxyethylidene (CH3-C-OH), acetaldehyde (CH3-CH:O), and vinyl alcohol (CH2:CH-OH). J Am Chem Soc 113(17):6452
11. Jursic BS (1999) Complete basis set ab initio exploring potential energy surface for triplet oxygen reaction with ethylene. THEOCHEM 492:85
12. Hu W, Lendvay G, Maiti B, Schatz GC (2008) Trajectory surface hopping study of the O(3P) + ethylene reaction dynamics. J Phys Chem A 112(10):2093
13. Joshi A, You X, Barckholtz Timothy A, Wang H (2005) Thermal decomposition of ethylene oxide: potential energy surface, master equation analysis, and detailed kinetic modeling. J Phys Chem A 109(35):8016
14. Yang X, Maeda S, Ohno K (2007) Insight into global reaction mechanism of [C2, H4, O] system from ab initio calculations by the scaled Hypersphere search method. J Phys Chem A 111(23):5099
15. Shepler BC, Braams BJ, Bowman JM (2008) "Roaming" dynamics in CH3CHO photodissociation revealed on a global potential energy surface. J Phys Chem A 112(39):9344
16. Heazlewood BR, Jordan MJT, Kable SH, Selby TM, Osborn DL, Shepler BC, Braams B, Bowman JM (2008) Roaming is the dominant mechanism for molecular products in acetaldehyde photodissociation. Proc Natl Acad Sci USA, Early Ed (Aug. 7 2008), p 1
17. Shepler BC, Braams BJ, Bowman JM (2007) Quasiclassical trajectory calculations of acetaldehyde dissociation on a global potential energy surface indicate significant non-transition state dynamics. J Phys Chem A 111(34):8282
18. Miyoshi A, Yoshida J-I, Shiki N, Koshi M, Matsui H (2009) Product branching fractions for the reaction of O(3P) with ethene. Phys Chem Chem Phys 11(33):7318
19. Gordon MS, Schmidt MW (2005) Advances in electronic structure theory: GAMESS a decade later. In: Dykstra CE, Frenking G, Kim KS, Scuseria GE (eds) Theory and applications of computational chemistry, the first forty years. Elsevier, Amsterdam, p 1167
20. Roos B (2007) The complete active space self-consistent field method and its applications in electronic structure calculations. In: Lawley KP (ed) Advances in chemical physics: ab initio methods in quantum chemistry Part 2, vol 69. Wiley, Inc., Hoboken, p 399

21. Ruedenberg K, Sundberg KR (1976) MCSCF studies of chemical reactions: natural reaction orbitals and localized reaction orbitals. In: Calais J-L, Goscinski O, Lindenberg J, Öhrn Y (eds) Quantum science, Plenum Publ. Co., New York. p 505
22. Schmidt MW, Gordon MS (1998) The construction and interpretation of MCSCF wavefunctions. Annu Rev Phys 49:233
23. Dunning TH Jr (1989) Gaussian basis sets for use in correlated molecular calculations. I. The atoms boron through neon and hydrogen. J Chem Phys 90(2):1007
24. Ivanic J, Ruedenberg K (2001) Identification of deadwood in configuration spaces through general direct configuration interaction. Theor Chem Acc 106(5):339
25. Lengsfield BH III (1980) General second order MCSCF theory: a density matrix directed algorithm. J Chem Phys 73:382
26. Dupuis M, Mougenot P, Watts JD (1989) In: Clementi E (ed) Modern Techniques in Theoretical Chemistry. ESCOM, Leiden
27. Yarkony DR (1981) Comment on the use of augmented Matrix in MCSCF Theory. Chem Phys Lett 77(3):634
28. Bauschlicher CW Jr (1980) The construction of modified virtual orbitals (MVO's) which are suited for configuration interaction calculations. J Chem Phys 72(2):880
29. Boys SF (1966) Localized orbitals and localized adjustment functions. In: Lödin P-O (ed) Quantum theory of atoms, molecules, and the solid state. A tribute to John C. Slater. Academic Press, New York, p 253
30. Gonzalez C, Schlegel HB (1989) An improved algorithm for reaction path following. J Chem Phys 90(4):2154
31. Hirao K (1992) Multireference Moeller-Plesset method. Chem Phys Lett 190(3–4):374
32. Piecuch P, Kucharski SA, Kowalski K, Musial M (2002) Efficient computer implementation of the renormalized coupled-cluster methods: the R-CCSD[T], R-CCSD(T), CR-CCSD[T], and CR-CCSD(T) approaches. Comput Phys Commun 149(2):71
33. Piecuch P, Wloch M (2005) Renormalized coupled-cluster methods exploiting left eigenstates of the similarity-transformed Hamiltonian. J Chem Phys 123(22):224105/1
34. Szalay PG, Bartlett RJ (1993) Multireference averaged quadratic coupled-cluster method: a size-extensive modification of multireference CI. Chem Phys Lett 214(5):481
35. Lischka H, Shepard R, Brown FB, Shavitt I (1981) New implementation of the graphical unitary group approach for multireference direct configuration interaction calculations. Int J Quantum Chem, Quantum Chem Symp 15:91
36. Lischka H, Shepard R, Pitzer RM, Shavitt I, Dallos M, Muller T, Szalay PG, Seth M, Kedziora GS, Yabushita S, Zhang Z (2001) High-level multireference methods in the quantum-chemistry program system COLUMBUS: analytic MR-CISD and MR-AQCC gradients and MR-AQCC-LRT for excited states, GUGA spin-orbit CI and parallel CI density. Phys Chem Chem Phys 3(5):664
37. Lischka H, Shepard R, Shavitt I, Pitzer RM, Dallos M, Mueller T, Szalay PG, Brown FB, Ahlrichs R, Boehm HJ, Chang A, Comeau DC, Gdanitz R, Dachsel H, Ehrhardt C, Ernzerhof M, Hoechtl P, Irle S, Kedziora G, Kovar T, Parasuk V, Pepper MJM, Scharf P, Schiffer H, Schindler M, Schueler M, Seth M, Stahlberg EA, Zhao J-G, Yabushita S, Zhang Z, Barbatti M, Matsika S, Schuurmann M, Yarkony DR, Brozell SR, Beck EV, Blaudeau J-P, Ruckenbauer M, Sellner B, Plasser F, Szymczak JJ (2008) In COLUMBUS, an ab initio electronic structure program, release 5.9.2. http://www.univie.ac.at/columbus
38. Hay PJ, Hunt WJ, Goddard WA III (1972) Generalized valence bond description of simple alkanes, ethylene, and acetylene. J Am Chem Soc 94(24):8293
39. Hunt WJ, Hay PJ, Goddard WA III (1972) J Chem Phys 57:738
40. Shepard R, Kedziora GS, Lischka H, Shavitt I, Mueller T, Szalay PG, Kallay M, Seth M (2008) The accuracy of molecular bond lengths computed by multireference electronic structure methods. Chem Phys 349(1–3):37
41. Bunge AV (1970) Electronic wavefunctions for atoms. III. Partition of degenerate spaces and ground state of carbon. J Chem Phys 53(1):20
42. Farazdel A, Dupuis M (1991) On the determination of the minimum on the crossing seam of two potential energy surfaces. J Comput Chem 12(2):276
43. Manaa MR, Yarkony DR (1993) On the intersection of two potential energy surfaces of the same symmetry. Systematic characterization using a Lagrange multiplier constrained procedure. J Chem Phys 99(7):5251
44. Yarkony DR (1993) Systematic determination of intersections of potential energy surfaces using a Lagrange multiplier constrained procedure. J Phys Chem 97(17):4407
45. Witek HA, Choe Y-K, Finley JP, Hirao K (2002) Intruder state avoidance multireference Moller-Plesset perturbation theory. J Comput Chem 23(10):957
46. Kozlowski PM, Davidson ER (1994) Considerations in constructing a multireference second-order perturbation theory. J Chem Phys 100(5):3672
47. Malrieu J-P, Heully J-L, Zaitsevskii A (1995) Multiconfigurational second-order perturbative methods: overview and comparison of basic properties. Theor Chim Acta 90(2/3):167
48. Nakano H (1993) Quasidegenerate perturbation theory with multiconfigurational self-consistent-field reference functions. J Chem Phys 99(10):7983
49. Marian CM (2001) Spin-orbit coupling in molecules. Rev Comput Chem 17:99
50. Fedorov DG, Koseki S, Schmidt MW, Gordon MS (2003) Spin-orbit coupling in molecules: chemistry beyond the adiabatic approximation. Int Rev Phys Chem 22(3):551
51. Yarkony DR (1992) Spin-forbidden chemistry within the Breit-Pauli approximation. Int Rev Phys Chem 11(2):195
52. Furlani TR, King HF (1985) Theory of spin-orbit coupling. Application to singlet-triplet interaction in the trimethylene biradical. J Chem Phys 82(12):5577
53. King HF, Furlani TR (1988) Computation of one and two electron spin-orbit integrals. J Comput Chem 9(7):771
54. Fedorov DG, Gordon MS (2000) A study of the relative importance of one and two-electron contributions to spin-orbit coupling. J Chem Phys 112(13):5611
55. Langhoff SR, Davidson ER (1974) Configuration interaction calculations on the nitrogen molecule. Int J Quantum Chem 8:61
56. Bruna PJ, Peyerimhoff SD (1981) The ground state of the CN + Ion: A multi-reference CI study. Chem Phys Lett 72:278
57. Ivanic J (2003) Direct configuration interaction and multiconfigurational self-consistent-field method for multiple active spaces with variable occupations. I. Method. J Chem Phys 119(18):9364
58. Chao J, Hall KR, Marsh KN, Wilhoit RC (1986) Thermodynamic properties of key organic oxygen compounds in the carbon range C1 to C4. Part 2. Ideal gas properties. J Phys Chem Ref 15(4):1369
59. Chase MW Jr (1998) NIST-JANAF thermochemical tables, 4th edn. J Phys Chem Ref Data Mongr 9. American Chemical Society, Washington, DC, pp 1–27
60. Wiberg KB, Crocker LS, Morgan KM (1991) Thermochemical studies of carbonyl compounds. 5. Enthalpies of reduction of carbonyl groups. J Am Chem Soc 113(9):3447
61. JANAF Thermochemical Tables (1985) Natl. Stand. Ref. Data Ser. U.S. National Bureau of Standards, Washington, DC, p 37
62. Ruscic B, Boggs J, Burcat A, Csaszar AG, Demaison J, Janoschek R, Martin JML, Morton ML, Rossi MJ, Stanton JF, Szalay PG, Westmoreland PR, Zabel F, Berces T (2005) IUPAC critical evaluation of thermochemical properties of selected radicals. Part I. J Phys Chem Ref Data 34(2):573
63. Cox JD, Wagman DD, Medvedev VA (1989) CODATA key values for thermodynamics